



Influence of grain size and plastic deformation on the phase transformation of enstatite: insights from microstructures produced during the back-transformation of protoenstatite to clinoenstatite

Miki Tasaka¹ · Maya Iwago¹

Received: 28 March 2024 / Accepted: 17 July 2024 / Published online: 5 August 2024
© The Author(s), under exclusive licence to Springer-Verlag GmbH Germany, part of Springer Nature 2024

Abstract

Enstatite ($\text{Mg}_2\text{Si}_2\text{O}_6$) is a member of the pyroxene group and an important mineral in the lower crust and upper mantle. Enstatite has three phases at ambient pressure: protoenstatite, orthoenstatite, and clinoenstatite. Previously, the polymorphic transformation of pyroxene has been characterized using bulk techniques such as X-ray diffraction of powders. Given that rocks are crystal aggregates, it is important to use aggregates to understand phase transformations. We therefore conducted grain growth and deformation experiments using aggregates of enstatite to investigate phase transformations. Grain growth experiments were conducted at temperatures (T) of 1345 and 1360 °C under a vacuum of ≈ 10 Pa using an alumina tube furnace. Deformation experiments were conducted at $T=1310$ °C and room pressure, a strain rate of $\approx 10^{-4}$ s⁻¹, and a resulting stress of ≈ 150 MPa. The samples were analyzed using a scanning electron microscope, electron backscatter diffraction (EBSD), and X-ray diffraction. The results indicate that the grain size affects the transformation from protoenstatite to clinoenstatite, whereas deformation by diffusion creep does not. The EBSD analyses show that the volume fraction of clinoenstatite increases with increasing grain size. The samples underwent diffusion creep during the deformation experiments, and there were no distinct microstructural differences between deformed and undeformed samples. The EBSD analyses show that the transformed clinoenstatite has a characteristic twin structure with a misorientation angle of 180° and a rotation axis of [100] or [001]. Grain sizes become smaller during the phase transformation, even if the mechanism can be characterized as a second-order transformation.

Highlights

- Grain growth and deformation experiments using aggregates of enstatite crystals were conducted to understand the microstructural developments due to the phase transformation from protoenstatite to clinoenstatite.
- Grain size influences the transformation, whereas deformation by diffusion creep does not.
- Grain sizes become smaller during the phase transformation, even if the mechanism can be characterized as a second-order transformation.

Keywords Enstatite · Phase transformation · Grain size · Stress · Twin

Introduction

Enstatite ($\text{Mg}_2\text{Si}_2\text{O}_6$) is a member of the pyroxene group and an important mineral in the lower crust and upper mantle. Enstatite has a complex of polymorphs, and their crystal structures change with pressure, temperature, and chemical composition (Lee and Heuer 1987; Ohi et al. 2010). Enstatite has three commonly observed polymorphs at ambient pressure: protoenstatite (PEn, space group Pbcn), stable at high temperatures ($T=985\text{--}1557$ °C); orthoenstatite (OEn,

✉ Miki Tasaka
tasaka.miki@shizuoka.ac.jp

¹ Department of geoscience, Shizuoka university, Shizuoka, Japan

Pbca), stable at moderate temperatures ($T=500\text{--}985\text{ }^{\circ}\text{C}$); and low-pressure clinoenstatite (CEn, $P2_1/c$), stable at low temperatures ($T\lesssim 500\text{ }^{\circ}\text{C}$), as described by Smyth (1974) and Ohi et al. (2022).

PEn is an unquenchable phase that transforms to twinned CEn in natural rocks (boninite and meteorites). Therefore, the typical occurrence of CEn and PEn in lower crustal and mantle rocks remain unclear. The stability field of PEn is within the range of $P<1\text{ GPa}$ and $T=985\text{--}1557\text{ }^{\circ}\text{C}$, and that of CEn is within the range of $P<7\text{ GPa}$ and $T\lesssim 500\text{ }^{\circ}\text{C}$ (e.g., Presnall 1995; Ohi et al. 2022). PEn crystals coexisting with CEn have also been observed in natural rocks such as boninite (Shiraki et al. 1980). Therefore, the transformation processes, microstructural changes, and kinetics of the back-phase transition of PEn are potentially important in constraining the thermo-dynamic processes and thermal history of these rocks.

PEn is the stable form at high temperatures, but the samples recovered from experiments can contain Pen, Oen, and/or CEn due to the back-transformation of PEn (Lee and Heuer 1987; Reynard et al. 2008). The back-transformation of PEn is influenced by grain size, shear stress, and cooling rate (Smyth 1974; Ohi et al. 2022). The strains related to the back-transformation of PEn due to cooling or ageing cause cracks in the recovered sample. Therefore, the polymorphic transformation of enstatite has been characterized using bulk techniques such as X-ray diffraction analyses of powder and single crystals (e.g., Lee and Heuer 1987; Jones et al. 1999; Ohi and Miyake 2016; Kanzaki and Xue 2017). However, rocks on Earth are aggregates of minerals, which affects the accommodation processes between adjacent grains, and this means that we should attempt to understand phase transformations using crystal aggregates.

High-spatial-resolution electron back-scattered diffraction (EBSD) now provides a method of analyzing the microstructural features of crystal aggregates of transformed CEn and OEn as well as remnants of PEn on the scale of hundreds of microns (Bystricky et al. 2024). Therefore, we conducted grain growth and deformation experiments using crystal aggregates of enstatite, and then investigated the microstructural features of the phase transformation of PEn to CEn using EBSD.

Methods

Sample preparation

Synthetic aggregates of enstatite and forsterite were used for the experiments. The aggregates contained 20 vol% forsterite to ensure silica activity was buffered and that grain size was kept small as a result of the pinning of secondary

grains (Hiraga et al. 2010a; Tasaka and Hiraga 2013). Sample preparation followed Koizumi et al. (2010). Nano-sized SiO_2 powder (particle size $\approx 30\text{ nm}$, purity $>99.9\%$) and $\text{Mg}(\text{OH})_2$ powder (particle size $\approx 50\text{ nm}$, purity $>99.98\%$) were mixed by milling for 24 h with iron-cored plastic balls and ethanol. The slurry was dried using a magnetic stirrer at $100\text{ }^{\circ}\text{C}$ for ~ 2 weeks. The powders were calcined in air at $1000\text{ }^{\circ}\text{C}$ for 3 h to synthesize enstatite and forsterite by a reaction of the two powders. The calcined powders were pulverized with an agate mortar and then shaped as a solid cylinder using a die of tungsten carbide. The sample was placed in the rubber sleeve that was evacuated using a vacuum pump. The vacuum-packed samples were dropped into a water pressure vessel with a cold (room temperature) isostatic pressure (CIP) of 150 MPa for 30 min. The cold-pressed cylindrical samples had diameters of $\approx 7\text{ mm}$ and heights of $\approx 15\text{ mm}$.

Grain growth experiments

The cold-pressed samples were sintered under a vacuum of $\approx 10\text{ Pa}$ using an alumina tube horizontal furnace. The samples were placed in a platinum boat to prevent reactions between samples and the alumina. The samples were sintered at temperatures of 1345 and 1360 $^{\circ}\text{C}$ and sintering times of 1, 5, 10, 50, and 100 h to produce samples with different grain sizes. At the end of each experiment, the temperature was decreased from 1345 $^{\circ}\text{C}$ to room temperature over 6 h at a rate of $4\text{ }^{\circ}\text{C min}^{-1}$.

Deformation experiments

The samples sintered at a temperature of 1345 $^{\circ}\text{C}$ for 10 h (sample 45S10) were used for the deformation experiments. All initial samples had a cylindrical shape with a diameter of $\approx 5\text{ mm}$ and height of $\approx 12\text{ mm}$. The samples were extremely dense (porosity $<1\text{ vol}\%$) fine-grained (average enstatite grain size of $2.7\text{ }\mu\text{m}$) crystal aggregates.

The deformation experiments were conducted under uniaxial compression in a mechanical testing machine (AGX-50kNV, Shimazu) set in a siliconite furnace at a pressure of one atmosphere. We collected force–displacement–time data at an interval of 1 s. The compressional force was measured by a load cell directly attached to the SiC loading rod, and the displacement was measured at the crosshead of the deformation apparatus. The load cell measured the force directly applied to the sample without frictional effects, thus allowing us to measure the force and displacement precisely. Similar types of deformation experiment have been conducted previously by our research group (e.g., Hiraga et al. 2010b; Tasaka et al. 2013, 2023).

The furnace temperature was increased from room temperature to 1310 °C at a rate of 10 °C/min. The samples were annealed for 20 min at 1310 °C to ensure a uniform temperature around the sample. The temperature was measured by an R-type thermocouple located adjacent to the sample, and the temperature was held constant within a range of ± 1 °C during the experiments. A constant displacement rate was applied using SiC loading rods until a true strain of ≈ 0.2 was reached. We conducted uniaxial compression experiments with strain rates of $\approx 1.0 \times 10^{-4}$ and $\approx 2.0 \times 10^{-4}$ s $^{-1}$, resulting in stresses of ≈ 125 and ≈ 165 MPa, respectively. The differential stress was calculated from the compressional force using the area change and assuming a constant volume and uniform strain during each experiment. The compressional strain was calculated from the displacement. A small piece of the sample was placed next to the deformed sample, but not in the deformation rods. We called these undeformed samples the reference samples, and they were made of the same materials as the deformed samples. By comparing deformation and reference samples with the same thermal history, we could distinguish the effects of the deformation. After each experiment, the temperature was decreased from 1310 °C to room temperature at a rate of 10 °C/min.

Microstructural analysis

The samples were polished using a diamond slurry with particle sizes of 15, 1.0, and 0.5 μm for 5 min each, and then polished with colloidal silica (~ 0.06 μm) for 5 min. The polished samples were thermally etched at 1210 °C and room pressure for 30 min to highlight the grain and phase boundaries. All the polished sections were prepared 1 day prior to SEM and EBSD analyses.

The polished sections had a carbon coating, and they were examined with a field emission–scanning electron microscope (FE-SEM; JSM-IT700HR, JEOL) along with an EDS detector (Ultim Max 170, Oxford Instruments) at Shizuoka University, Japan. Secondary electron images (SEI) and energy dispersion X-ray spectroscopy (EDS) maps were obtained for the same area on each section, so that grain boundary and compositional differences could be identified for the enstatite and forsterite grains. The outlines of the grains were manually traced. The equivalent-area diameter (d_i) was calculated from the grain area (A) using $d_i = 2(A/\pi)^{0.5}$. The average grain sizes of the enstatite and forsterite were then calculated (arithmetic mean) using the equivalent-area diameters without a scaling factor (e.g., $4/\pi$). The enstatite grain size derived from SEM + EDS analysis is referred to as the prior PEn grain size. Minimal microstructural changes (grain size and grain shape of prior enstatite) occurred during thermal etching, as was evidenced by

comparing EBSD analyses of the samples with and without thermal etching. The minimum grain size measured by this method is ≈ 0.1 μm . The grain sizes, including one standard deviation of the mean (SD), the number of analyzed grains (N), and the enstatite (prior PEn) volume fraction (f_{En}), are summarized in Table 1.

Phase identification

X-ray diffraction (XRD) and EBSD were used to identify enstatite phases. The XRD (SmartLab CA-1320 A, Rigaku) analyses were conducted at Shizuoka university using Cu K_α radiation. The analytical conditions were diffraction angles from 15° to 70° with scanning step intervals of 0.01°, voltage of 40 kV, and current of 30 mA. A non-refractive silicon standard was used for calibrations before and after the analyses to ensure reproducibility of peak positions.

The crystallographic orientations of the forsterite, CEn, and PEn were measured using EBSD. Polished sections (without coating or thermal etching) were analyzed with a field emission–scanning electron microscope (FE-SEM; JSM-IT700HR, JEOL) equipped with an EBSD detector (Symmetry S2, Oxford Instruments) at Shizuoka University. The EBSD analyses were conducted with a tilt angle of 70°, acceleration voltage of 15 kV, probe current of ≈ 5 nA, working distance of ≈ 30 mm, vacuum of more than ≈ 50 Pa, magnification of $\times 4000$, and grid spacing of 0.1 μm . A Hough transformation was employed to identify the Kikuchi band. The binned pattern size used for the Hough transform was 1244×1024 pixels, and the theta step size was $\sim 3^\circ$. A butterfly filter was used to process the final Hough pattern. The maximum and minimum numbers of bands were 11 and 7, respectively. The index files of protoenstatite, clinoenstatite, and forsterite were used (HKL and American Mineralogist crystal structure database). The lattice parameters for the analyses were as follows: (a, b, c, α , β , γ) = (9.3060, 8.8860, 5.3600, 90, 90, 90) for PEn, (9.7730, 8.9620, 5.2710, 90, 109, 90) for CEn, and (4.7560, 10.2070, 5.9800, 90, 90, 90) for forsterite.

Noise reduction procedures were applied to the orientation maps using AZtecCrystal (version 2.2). Non-indexed empty pixels with ≥ 6 indexed nearest neighbors within the same grain were assigned the average orientation of the neighboring pixels. Isolated indexed pixels were excluded, as they were probably produced by analytical errors during analysis. The Kuwahara filter was applied to remove orientation noise. The index rates of the raw data for the EBSD maps ranged from 73 to 94%. After noise reduction, 83–98% of the area of each map could be indexed, so that we were able to determine mineral fractions and grain sizes precisely.

Table 1 Grain size from SEM + EDS analysis grain growth experiments

sample name	T °C	time h	enstatite (prior PEn)			forsterite			mineral fraction		
			dEn_avg μm	SD	N	dFo_avg μm	SD	N	fEn %	fFo	
4SS1	1345	1	1.72	0.96	237	0.84	0.40	359	74.73	25.27	
4SS5	1345	5	2.54	1.21	139	1.23	0.55	188	76.31	23.69	
4SS10*	1345	10	2.69	1.10	118	1.31	0.52	176	74.14	25.86	
4SS50	1345	50	3.76	1.32	99	1.63	0.67	124	80.27	19.73	
60S1	1360	1	1.78	0.85	83	0.97	0.37	131	69.46	30.54	
60S10	1360	10	exploded								
60S50	1360	50	exploded								
60S100	1360	100	exploded								
deformation experiments											
sample name	T °C	strain rate ×10 ⁻⁴ s ⁻¹	dEn_avg μm	SD	N	forsterite dEn_avg μm	SD	N	fEn %	fFo	
4SS10_D1	1310	1	2.54	1.3	268	1.19	0.53	367	77.93	22.07	
4SS10_D1r	1310		2.99	1.4	101	1.19	0.59	181	77.71	22.29	
4SS10_D2	1310	2	2.30	1.2	342	1.06	0.49	477	77.63	22.37	
4SS10_D2r	1310		3.02	1.4	105	1.31	0.50	155	79.33	20.67	
dEn_avg	average grain size of enstatite										
dFo_avg	average grain size of forsterite										
SD	standard deviation										
N	the number of analyzed grains										
T	temperature										

*initial sample for deformation experiments

Mineral fractions of forsterite, PEn, and CEn were determined by EBSD analysis, using the area of each phase. Non-indexed pixels were excluded when calculating the mineral fractions. Most of the non-indexed areas were located along grain boundaries and cracks. The twins in CEn, with a rotation axis of [001] or [100] and a rotation angle of $180 \pm 5^\circ$, were excluded from the grain size analyses of CEn, as they could be transformation twins, as described later. The enstatite grain size derived from EBSD analysis is referred to as the current PEn grain size. Grain boundaries were defined as having misorientation angles of $> 10^\circ$, and sub-grain boundaries were defined as having misorientation angles of 2° – 10° . Grains comprising ≥ 10 pixels were used for grain size and crystallographic orientation analyses to exclude poorly indexed grains (e.g., grains with a speckled appearance in Figs. 2, 3, S2, and S3). As a result of these steps, the results are unlikely to have been affected by the mis-indexing of enstatite grains.

Results

Results of grain growth experiments

The samples sintered at 1360°C for > 1 h exploded after a certain time (several hours to days) and became powders, as shown in Fig. S1b–d. We observed the sample sintered at 1360°C for 10 h using a video camera at room temperature and pressure (*PT*) to see how the sample exploded (Supplementary material video 1). At first, the center of the sample became whitish in color. Then, the size of the sample expanded, and the edge of the sample broke away in pieces. After 8 days, the sample was completely powdered (Fig. S1). The powders derived from the exploded samples were analyzed using XRD to identify the mineral phases. The other samples were transparent and retained their cylindrical shapes after the experiments (Fig. S1a, e–h), and these samples were cut and polished following the method outlined in Sect. 2.4, and then analyzed by SEM and EBSD.

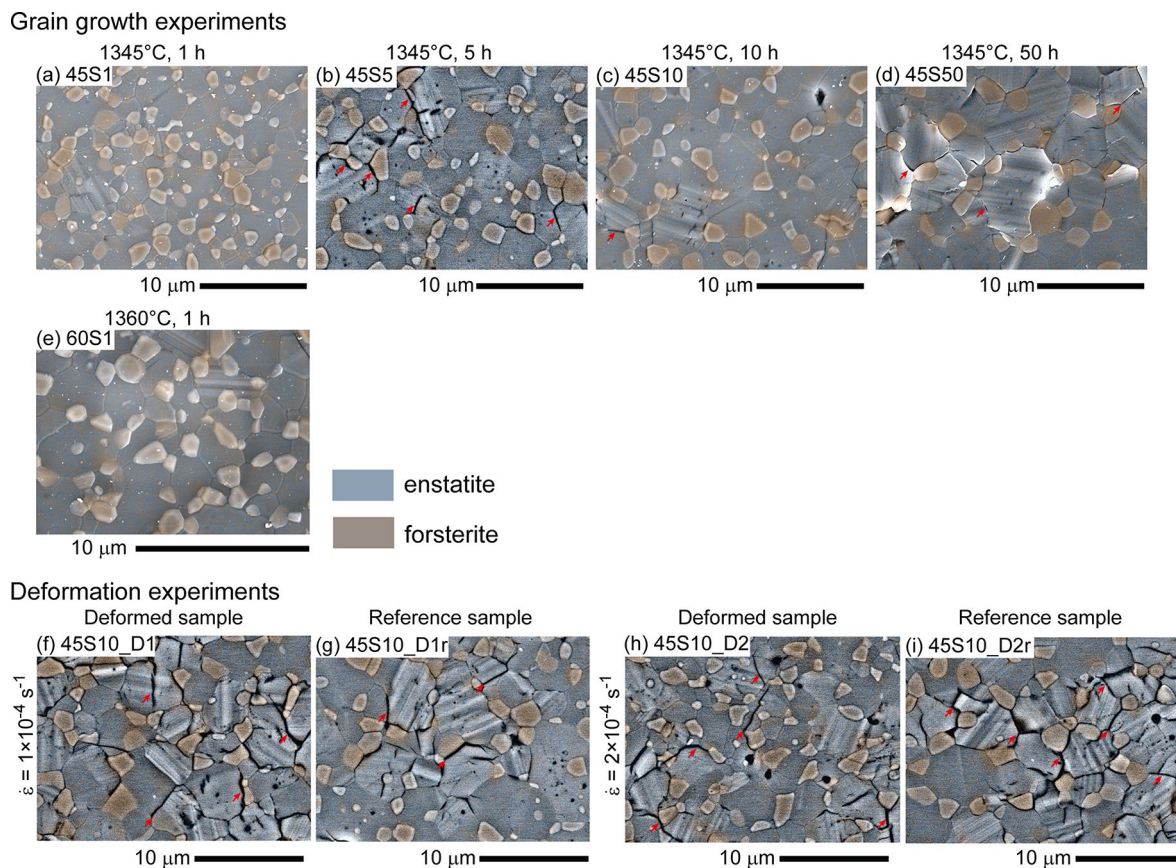


Fig. 1 (a–e) SEM images with superimposed EDS maps for samples in the grain growth experiments with sintering times of (a) 1 h, (b) 5 h, (c) 10 h, and (d) 50 h at a temperature of 1345°C , and (e) a sintering time of 1 h at 1360°C . (f) SEM image with EDS map of a sample from a deformation experiment with a strain rate of $1 \times 10^{-4} \text{ s}^{-1}$ and (g) a

reference sample. (h) Image of a sample from a deformation experiment with a strain rate of $2 \times 10^{-4} \text{ s}^{-1}$ and (i) a reference sample. The blue minerals are enstatite, and the gray minerals are forsterite. The grain boundaries around the enstatite grains with cracks are indicated by red arrows

Microstructures

The SEM images and EDS maps of samples with sintering times of 1 to 50 h at temperatures of 1345 and 1360 °C are shown in Fig. 1a–e. The images demonstrate that the samples are dense (porosity < 1 vol%) and that the enstatite and forsterite grains are distributed homogeneously. The grain size of enstatite (prior PEn) increased from 1.72 to 3.76 μm with increasing sintering time from 1 to 50 h at 1345 °C (Fig. 1a–d; Table 1). The enstatite grains are twinned, and the grain boundaries around some of the enstatite grains contain cracks (Fig. 1). Inter-granular, intra-granular, and trans-granular cracks were observed around enstatite grains. These microstructural features are consistent with those observed previously by our research group using the same method of sample preparation (Tasaka and Hiraga 2013).

EBSD analyses

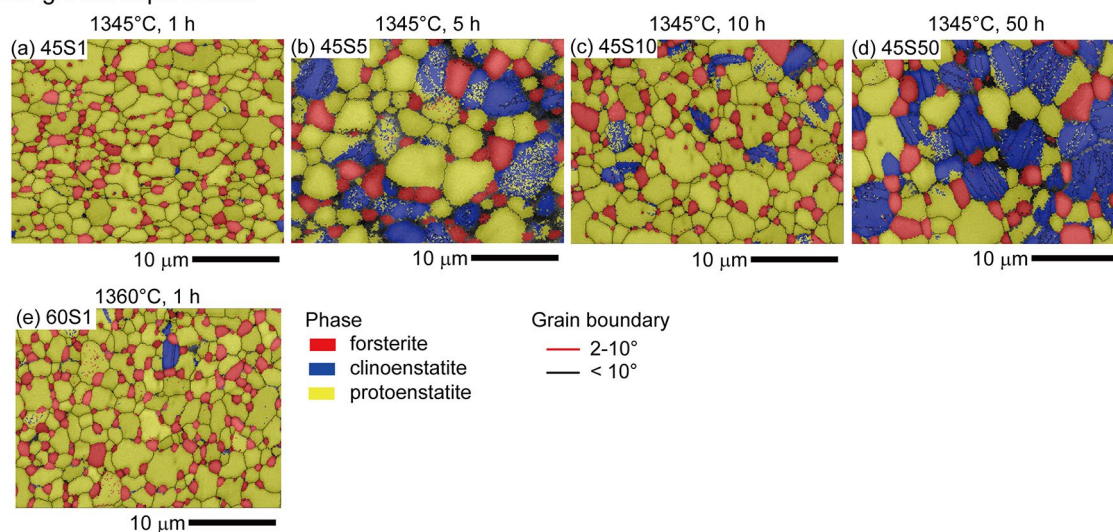
EBSD maps of samples with sintering times of 1 to 50 h at 1345 °C are shown in Fig. 2 and S2. The mineral fractions of PEn, CEn, and forsterite, as determined by EBSD analyses

(Fig. 2; Tables 1 and 2), indicate that the volume fraction of CEn increases with increasing grain size. For example, $f_{\text{CEn}} = 0\%$ with a prior PEn grain size of 1.72 μm in sample 45S1, whereas $f_{\text{CEn}} = 41\%$ with a prior PEn grain size of 3.76 μm in sample 45S50. On the other hand, the fraction of PEn decreases with increasing grain size. For example, $f_{\text{PEn}} = 82\%$ with a prior PEn grain size of 1.72 μm (45S1), whereas $f_{\text{PEn}} = 40\%$ with a prior PEn grain size of 3.76 μm (45S50). The fraction of forsterite is constant (17 to 18 vol%), regardless of sintering time and grain size.

Most of the CEn grains are twinned (Fig. 3, S2, S3). Pole figures of PEn and forsterite from EBSD analyses (Fig. S4) indicate uniform distributions in the CPOs (weak CPO) with small fabric intensities ($J \sim 3$). CEn shows a strong fabric intensity ($J = 6$ to 10), probably due to the small number of grains analyzed. Microstructural data for all samples are summarized in Table 2.

The grain orientation spread (GOS) maps from the EBSD analyses of samples with sintering times of 1 and 50 h at 1345 °C (samples 45S1 and 45S50) are shown in Fig. 3. The sample with sintering times of 50 h (45S50) had sufficient CEn grains ($N > 100$) for the analysis. The PEn grains have

Grain growth experiments



Deformation experiments

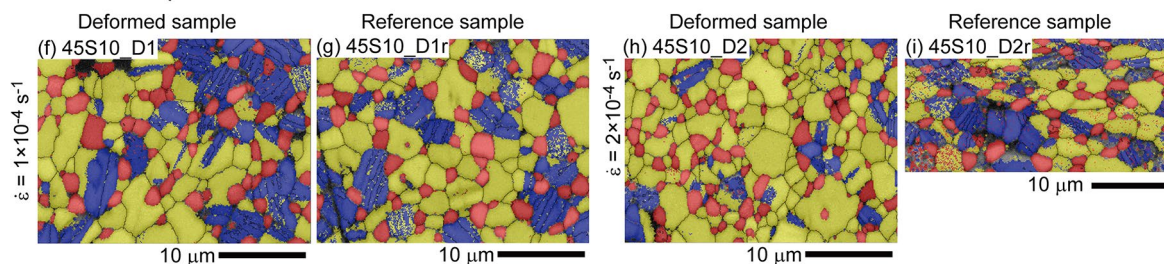


Fig. 2 (a–e) EBSD maps of samples from grain growth experiments with sintering times of (a) 1 h, (b) 5 h, (c) 10 h, (d) 50 h at 1345 °C, and (e) 1 h at 1360 °C. (f) EBSD map of a sample in a deformation experiment with a strain rate of $1 \times 10^{-4} \text{ s}^{-1}$ and (g) a reference sample. (h)

EBSD image of a sample from a deformation experiment with a strain rate of $2 \times 10^{-4} \text{ s}^{-1}$ and (i) a reference sample. The phase map indicates the phase distribution

Table 2 Microstructural data from EBSD analysis

grain growth experiments sample name	<i>T</i> °C	time h	mineral fraction f_{PEn} %	f_{CEn}	f_{Fo}	<i>N</i>	average value			SD			aver- age value			aver- age value										
							grain size μm	PEn**	CEn	Fo	grain size	PEn	CEn	Fo	shape factor	PEn	CEn	Fo	GOS	MOS						
45S1	1345	1	82	0	18	224	4	201	1.67	0.67	0.84	0.83	0.34	1.81	2.37	1.45	1.22	1.11	1.12	0.47	0.51	0.43	2.51	1.65	1.53	
45S5	1345	5	55	25	21	101	38	51	1.59	1.70	1.50	1.34	1.52	0.84	1.79	1.57	1.67	1.27	1.42	1.23	0.50	0.56	0.51	2.11	2.32	2.17
45S10*	1345	10	74	7	20	156	22	125	1.80	1.30	1.08	1.06	0.89	0.52	1.80	2.08	1.49	1.27	1.42	1.14	0.50	0.53	0.44	2.08	2.40	1.67
45S50	1345	50	40	41	19	65	136	48	1.94	1.35	1.66	1.30	0.92	0.84	1.85	2.83	1.66	1.30	1.70	1.18	0.46	0.49	0.47	1.98	1.81	2.07
60S1	1360	1	77	2	22	182	5	179	1.81	1.24	0.99	0.9	0.71	0.37	1.82	2.93	1.61	1.25	1.41	1.14	0.45	0.46	0.46	2.01	1.94	1.7
60S10	1360	10	exploded																							
60S50	1360	50	exploded																							
60S100	1360	100	exploded																							
deformation experiments* sample	<i>T</i> °C	strain rate $\times 10^{-4} s^{-1}$																								
45S10_D1**	1310	1	47	31	21	80	130	85	1.96	1.19	1.35	1.17	0.80	0.62	1.93	2.65	1.65	1.27	1.38	1.19	0.57	0.58	0.50	2.67	2.17	2.16
45S10_D1r	1310		51	29	20	112	145	77	1.62	1.72	1.42	1.20	1.27	0.56	1.86	1.83	1.45	1.27	1.50	1.16	0.69	0.76	0.66	2.34	2.59	2.55
45S10_D2**	1310	2	69	11	20	141	69	117	1.84	1.02	1.16	1.06	0.58	0.48	1.84	2.77	1.67	1.27	1.36	1.16	0.65	0.70	0.50	2.71	2.13	1.86
45S10_D2r	1310		45	32	23	96	79	111	1.33	1.11	0.95	0.90	0.91	0.45	2.34	2.03	1.90	1.27	1.32	1.22	0.94	0.84	0.78	3.03	2.60	2.59

* Mineral fraction before the deformation experiments

** Mineral fraction after the deformation experiments

***current PEEn grain size

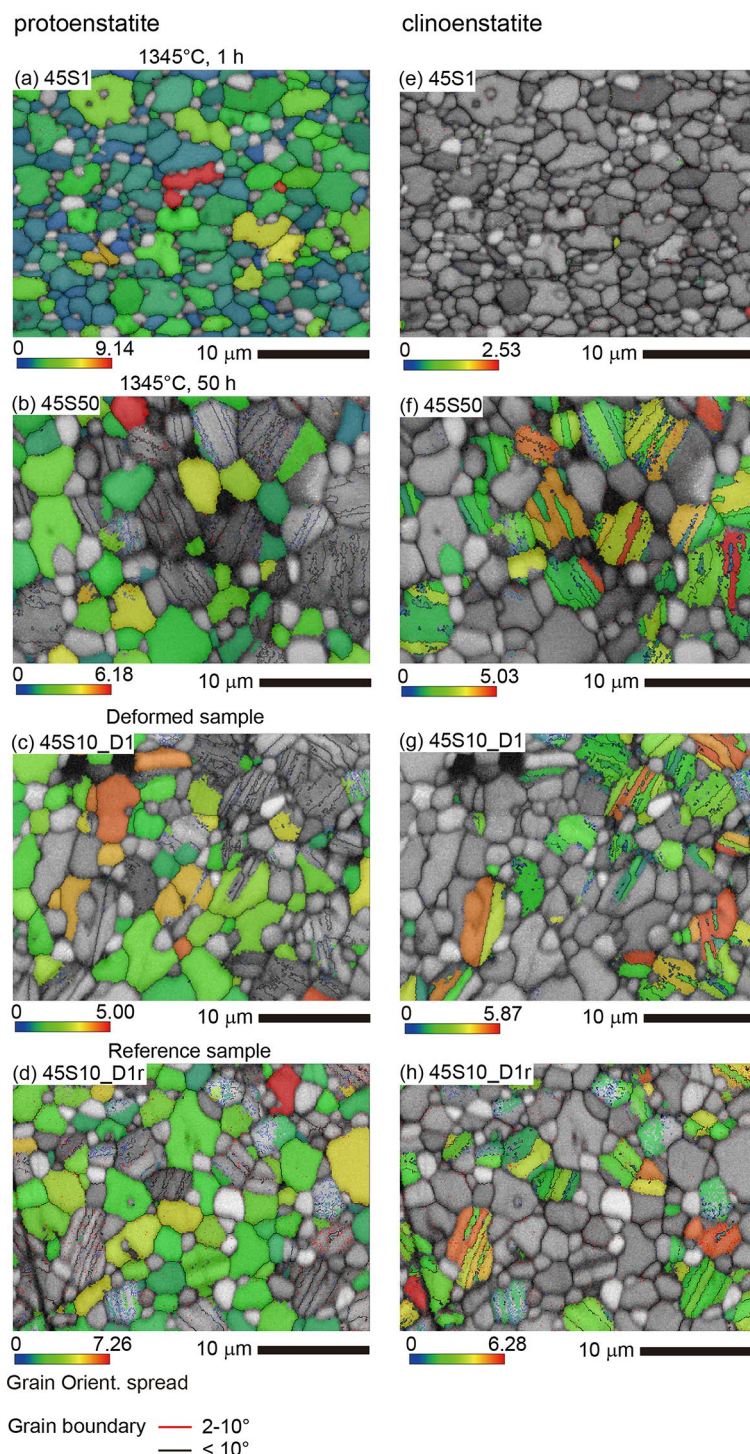
GOS: Grain Orientation Spread

MOS: Maximum Orientation Spread

SD: Standard deviation of the mean

shape factor: perimeter / equivalent perimeter

Fig. 3 (a, b, e, f) Grain orientation spread (GOS) maps with superimposed band contrast image of EBSD analyses from grain growth experiments with sintering times of (a, e) 1 h and (b, f) 50 h at 1345 °C. (c, d, g, h) Map from EBSD analysis of deformed and reference sample from a deformation experiment with a strain rate of $1 \times 10^{-4} \text{ s}^{-1}$. The maps in the left column are for protoenstatite (a–d), and those in the right column are for clinoenstatite (e–h)

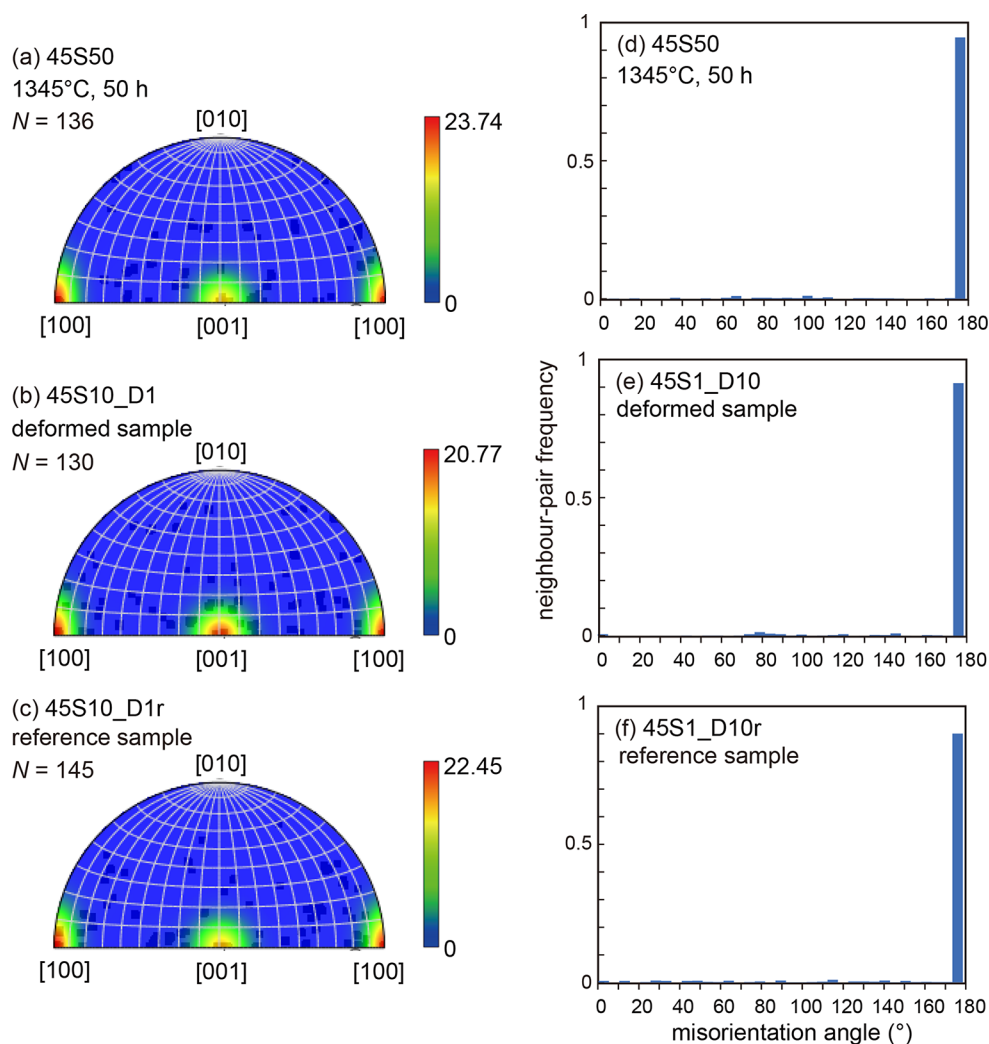


smaller GOS ($0\text{--}3^\circ$), whereas some grains have high larger GOS ($5\text{--}9^\circ$) (Fig. 3ab). In contrast, the CEn grains have twins with GOS angles of $1\text{--}5^\circ$ (Fig. 3f).

The misorientation angles and misorientation axes between neighboring grains were analyzed for the CEn crystals (Fig. 4). The samples with sintering times of 50 h (sample 45S50) were analyzed because the EBSD maps for these samples had sufficient CEn grains ($N > 100$). The

inverse pole figures of misorientation axes for neighboring grains (Fig. 4a) demonstrate that the rotation axes for neighboring grains are concentrated on $[100]$ or $[001]$. The histograms of misorientation angles for neighboring pairs show peaks at 180° (Fig. 4d). These features imply that the grains have characteristic twin boundaries with $[100]$ or $[001]$ rotation axes and rotation angles of 180° . These

Fig. 4 (a–c) Misorientation axes for neighboring CEn grains. (d–f) Misorientation angles for neighboring CEn grains. The samples were analyzed because the EBSD maps from these samples provided sufficient CEn grains ($N > 100$). (a, d) Inverse pole figures and misorientation angle distributions for samples from grain growth experiments with sintering times of 50 h at 1345 °C. (b, c, e, f) Inverse pole figures and misorientation angle distributions from the deformation experiments with strain rates of $1 \times 10^{-4} \text{ s}^{-1}$ for deformed and reference samples



twin structures in the CEn are consistent with previously reported TEM observations (Buseck et al. 1980 and reference therein).

Grain size distributions

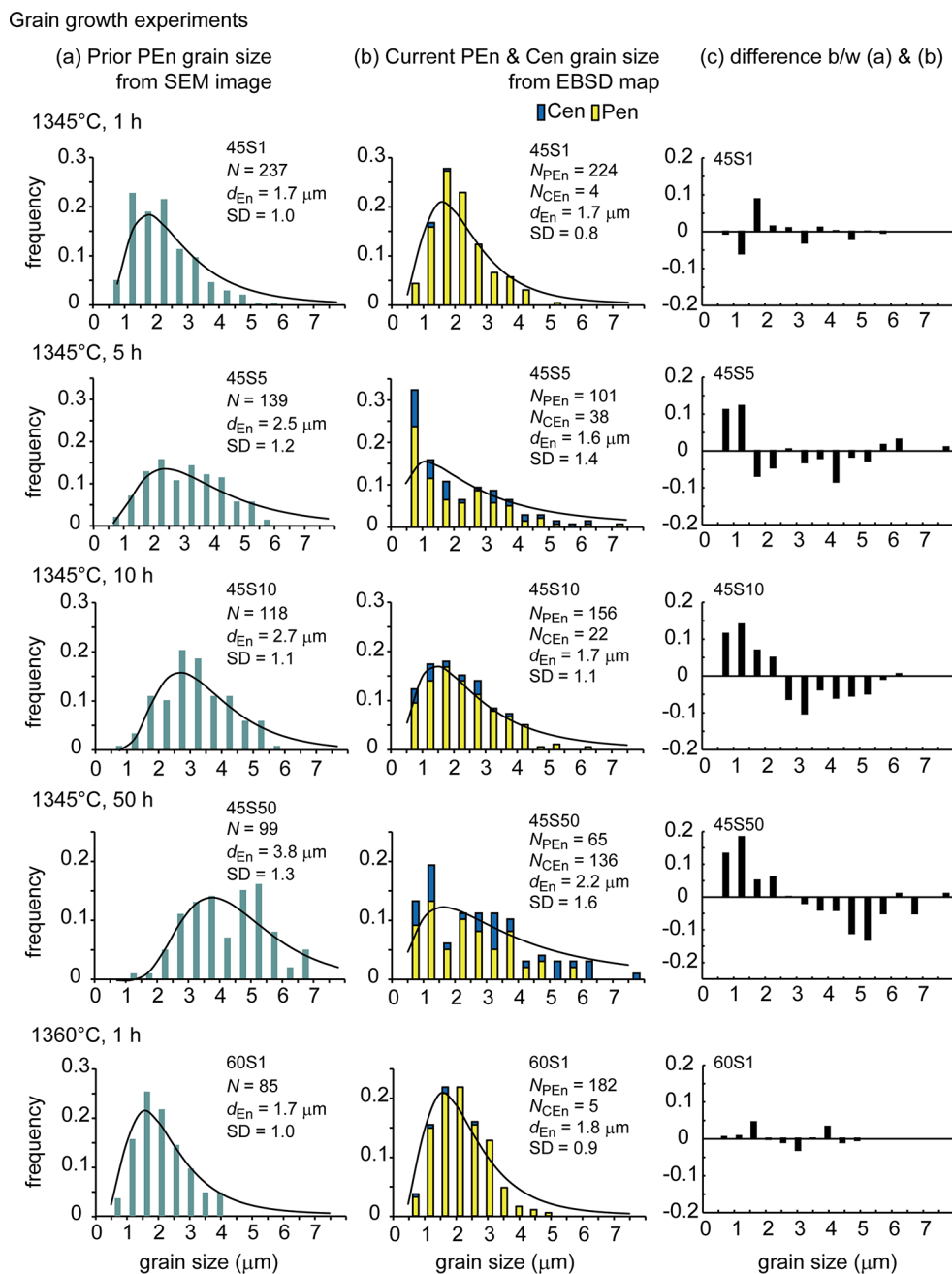
The grain size distributions of prior PEn grains derived from SEM+EDS analyses (Fig. 5a, S5) are similar to log-normal distributions, and the average grain size increases with increasing sintering time. The grain size distributions of current PEn and CEn, as derived from EBSD analyses, are shown in Fig. 5b. The distribution is log-normal in the sample with a sintering time of 1 h. In contrast, when comparing the calculated log-normal distributions derived from the average grain size and one standard deviation from the mean, a higher frequency of smaller grains occurs in samples with longer sintering times of 5 and 50 h (samples 45S5 and 45S50 in Fig. 5b). The differences between the grain size distributions of prior PEn and current PEn and CEn are shown in Fig. 5c. The distributions derived using

different methods for the sample with a sintering time of 1 h at 1345 °C (sample 45S1) have a similar trend of average grain size, and a standard deviation of the mean (Fig. 5ab). In contrast, the samples with sintering times of > 5 h show EBSD-derived distributions (current PEn and CEn) with a higher frequency of smaller grains and a lower frequency of larger grains than those derived from SEM+EDS analyses (prior PEn). The differences become larger with increasing grain size and sintering time. The boundary between positive and negative values in Fig. 5c occurs at a grain size of $\approx 3 \mu\text{m}$, as is clear in the sample with a sintering time of 50 h.

X-ray diffraction data

The powders derived from the exploded samples with sintering times of > 1 h at 1360 °C were analyzed using XRD to identify the mineral phases (Fig. 6b–d). The calcined powders that were annealed at 1360 °C for 1 h using a vacuum furnace were also analyzed for comparison (Fig. 6a).

Fig. 5 (a) Enstatite grain size distributions derived from SEM and EDS images (prior PEn grain sizes). The solid lines indicate the theoretical log-normal grain size distributions calculated for the average grain size and standard deviation. (b) PEn and CEn grain size distributions derived from EBSD maps (current PEn and CEn grain sizes). The solid lines are the log-normal distributions calculated the same way as for (a). (c) Differences in distribution between (a) and (b). The positive values indicate that the grains could be detected by EBSD but not by SEM. The negative values indicate that the grains could be detected by SEM, but not by EBSD. N = the number of analyzed grains. SD = standard deviation of the mean



The powders annealed at 1360 °C for 1 h show peaks for PEn and forsterite, and the absence of CEn in the sample is consistent with our EBSD analyses (Fig. 1e). In contrast, the samples with sintering times of 10, 50, and 100 h show peaks of CEn and forsterite but an absence of PEn peaks (Fig. 6b–d).

Results of the deformation experiments

Mechanical data

The relationship between strain and stress (Fig. 7a) demonstrates that stress increases with increasing strain, and that a steady-state flow stress was reached at a strain of ≈ 0.06 . The steady-state flow stress was 125 MPa for a true strain of 0.23 and a strain rate of $1.1 \times 10^{-4} \text{ s}^{-1}$, and 166 MPa for a true strain of 0.17 and a strain rate of $1.9 \times 10^{-4} \text{ s}^{-1}$. The steady-state flow stress was almost constant within ± 5 MPa, and no strain weakening or hardening was observed at strains

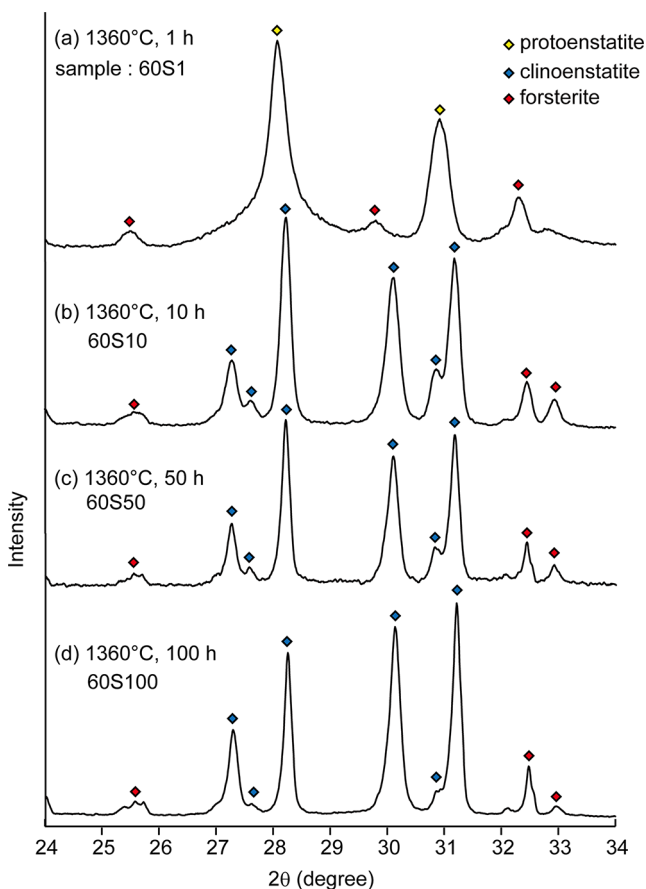


Fig. 6 (a) XRD patterns of powders annealed at 1360 °C for 1 h using a vacuum furnace. (b–d) XRD patterns of exploded samples with sintering times of (b) 10 h, (c) 50 h, and (d) 100 h at a temperature at 1360 °C. Peaks for protoenstatite, clinoenstatite, and forsterite are indicated by different colored symbols

of >0.1 . These features are consistent with the mechanical properties reported in our previous study (Tasaka et al. 2013).

Microstructures

In the microstructural analyses (Figs. S2–S6; Table 1, and 2), we were unable to detect microstructural differences between the deformed and reference samples in terms of grain size, grain shape, phase distribution. The microstructural features are consistent with those observed in the grain growth experiments, as described in Sect. 3.1.1 to 3.1.3. Exceptions were made for the deformation experiments with $\dot{\epsilon} = 2 \times 10^{-4} \text{ s}^{-1}$ (samples 45S10D2 and 45S10D2r). The prior grain sizes of PEn were different for the deformed and reference samples (2.30 and 3.02 μm , respectively).

Discussion

In general, there are two types of phase transformation mechanism (e.g., Karato 2008). A first-order phase transformation occurs because the first derivatives of Gibbs free energy change. This type of transformation is accompanied by diffusional processes, and grain sizes change. A second-order phase transformation does not involve a change in grain size and does not require a diffusional process. The transformation from PEn to CEn, the α to β transformation of quartz, and many structural transformations of perovskite also belong to the second type. The microstructural changes associated with the back-phase transition of PEn observed in this study are discussed in the following sections.

Grain size versus mineral fraction

The grain sizes derived from SEM + EDX provide an estimate of the prior PEn grain size at a high temperature. In contrast, the grain sizes from EBSD measurements represent the current PEn grain size. SEM + EDS analyses provide data only on compositional differences, while EBSD provides crystallographic orientations including the differences between PEn and CEn (Figs. 1 and 2). The SEM and EBSD images of the samples sintered for 1 h show that the grain size distributions of prior PEn and current PEn are almost identical, which is consistent with this inference (samples 45S1 and 60S1 in Fig. 5). The resolution of grain size analyses is similar for SEM + EDS and EBSD analyses, as shown by the similar grain size distributions, average grain sizes, and standard deviations of the mean for the samples with a sintering time of 1 h (Fig. 5).

The probability of transformation of PEn increases with increasing grain size above the threshold, as inferred from a comparison of samples with different enstatite grain sizes. The mineral fractions of PEn and CEn show a relationship with the grain size of prior PEn (Fig. 8a). The fraction of PEn reaches 50% at the prior PEn grain size of $\approx 3.5 \mu\text{m}$. The grain size distributions given by SEM and EBSD analyses (Fig. 5c) also demonstrate that the threshold value for the transformation from PEn to CEn is a grain size of $\approx 3 \mu\text{m}$. The threshold value is likely to be constant regardless of annealing time and temperature within our experimental conditions.

In the GOS maps from the EBSD analyses (Fig. 3, S3), most of the PEn grains have lower GOS values (0° – 3°), while some have higher angles (5° – 9°). The PEn grains with high GOS values indicate that the grains with a similar orientation are in contact with each other. The misorientation at the grain boundary is smaller than the value used to define separate grains ($<10^\circ$), and these grains may eventually transform to CEn.

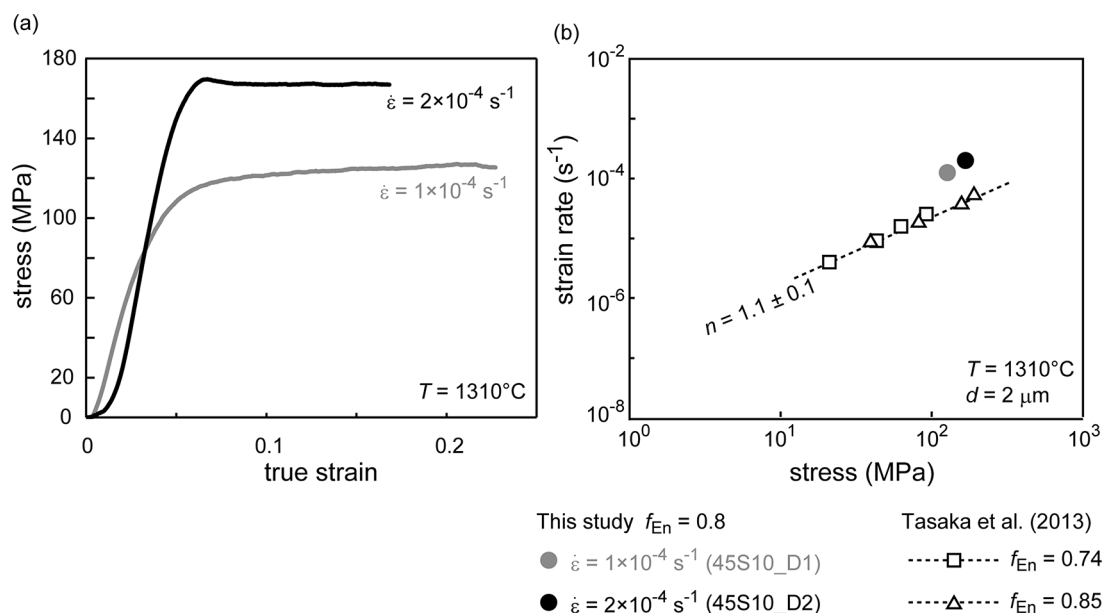


Fig. 7 (a) Relationship between stress and true strain at a temperature of 1310°C . The gray line indicates data for a strain rate of $1 \times 10^{-4} \text{ s}^{-1}$ and the black line indicates data for a strain rate of $2 \times 10^{-4} \text{ s}^{-1}$. (b) Relationship between strain rate and stress. The gray circle indicates a steady-state stress and a strain rate of $1 \times 10^{-4} \text{ s}^{-1}$, and the black circle indicates data for a strain rate of $2 \times 10^{-4} \text{ s}^{-1}$. Open symbols indicate data from Tasaka et al. (2013), which are shown for comparison. Tasaka et al. (2013) conducted a series of deformation experiment with

different temperatures, stresses, and grain sizes, and concluded that the samples were deformed by grain boundary diffusion creep with $n \sim 1$ and $p \sim 2$ (i.e., $\dot{\epsilon} \propto \sigma^n d^{-p}$). Therefore, the data are normalized to a grain size of $d = 2 \mu\text{m}$ with a grain size exponent of $p = 2$. The dotted line is the best-fit line using the data from Tasaka et al. (2013). The slope indicates the stress dependence of the strain rate, $n = 1.1 \pm 0.1$. $f_{\text{En}} = \text{enstatite volume fraction}$

Relationships between phase transformations and grain size

Grain size influences the phase transformation from PEn to CEn, because the defects that enable the transformation can change with grain size. The phase transformation occurs from lattice defects (i.e., point and/or linear defects) that reduce the distortional strain energy induced by transformation. Chen et al. (1985) discussed the statistics of martensitic nucleation models, and Ohi et al. (2022) applied the nucleation model to clarify the conditions under which PEn is retained at room PT . The fraction of PEn remaining at room PT during cooling is described as follows:

$$f_{\text{PEn}} = \exp(-Cd^m) \quad (1)$$

where C is a constant, d is grain size, and m is the number of dimensions of defect dispersion, with $m = 1, 2,$ or 3 for point, surface, and volume nucleation, respectively. The transformation from PEn to CEn is thought to be martensitic in nature (Smyth 1974; Lee and Heuer 1987).

The relationship between enstatite grain size and the fraction of retained protoenstatite is shown in Fig. 8b. Data from a previous study (Ohi et al. 2022) are added for comparison. The best-fit curves are shown for $m = 1, 2,$ and 3 , using our data and assuming Eq. (1). The model with $m = 3$ applies

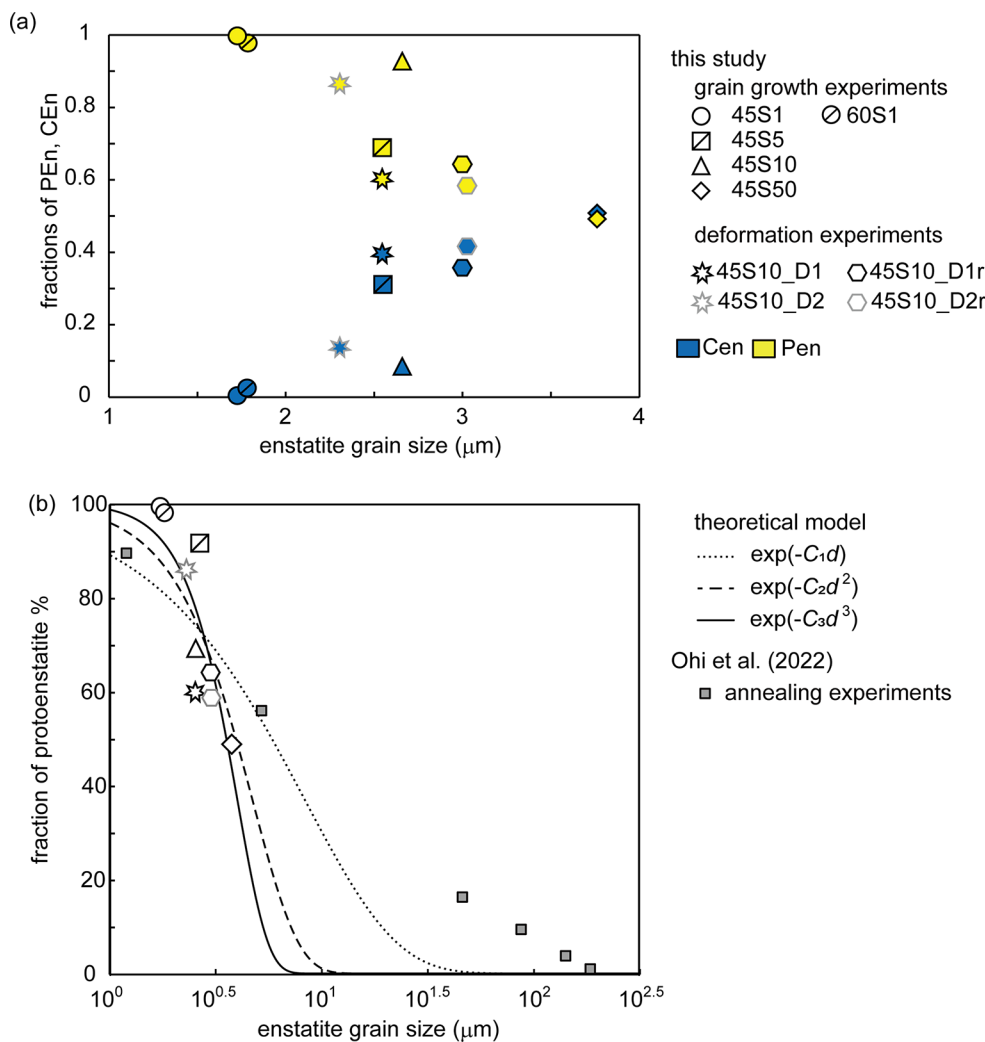
best to our results based on the residual sum of squares. The value of $m = 3$ indicates that the phase transformation from PEn to CEn occurs as a volume nucleation (i.e., nucleation in the volume of the lattice) or in a three-dimensional defect.

Effects of deformation on the phase transformation

The relationship between stress and strain rate is shown in Fig. 7b, with experimental data from our previous study added for comparison (Tasaka et al. 2013). Tasaka et al. (2013) conducted deformation experiments at 1310°C with the same enstatite + forsterite crystal aggregates (enstatite fraction, $f_{\text{En}} = 0.74$ or 0.85) as in the present study, using the same sample preparation procedures and a similar type of deformation apparatus. The stress and strain rate data derived from our new and previous studies differ by $\leq 15\%$. The $\leq 15\%$ difference between this and previous studies was probably derived from the grain size correction. It is difficult to accurately specify the grain size exponent of p ($\dot{\epsilon} \propto d^{-p}$) because we cannot vary the grain size by more than one order of magnitude for a given deformation mechanism.

Deformation by diffusion creep has no additional effect on the PEn–CEn transition under the experimental conditions of this study. We did not detect microstructural differences between the deformed and reference samples in terms of grain shape, phase distribution, and crystallographic

Fig. 8 (a) Relationship between the mineral fractions of PEn and CEn ($f_{\text{PEn}}, f_{\text{CEn}}$) and enstatite grain size (prior PEn grain size). The data are provided in Table 2. The fraction of PEn and CEn were calculated as follows: $f_{\text{PEn}}/(f_{\text{PEn}} + f_{\text{CEn}})$ and $f_{\text{CEn}}/(f_{\text{PEn}} + f_{\text{CEn}})$, respectively. (b) Relationship between the fraction of protoenstatite derived from EBSD analyses and the prior PEn grain size. The fraction of protoenstatite was calculated as follows: $100 \times f_{\text{PEn}}/(f_{\text{PEn}} + f_{\text{CEn}})$. The different symbols indicate different experiments. Gray square symbols indicate data from Ohi et al. (2022), which are shown for comparison. The theoretical model represented by Eq. (1) is shown by dotted, dashed, and solid lines for $m = 1, 2,$ and $3,$ respectively. The best-fit C values for Eq. (1) are $C_1 = 1.20 \times 10^{-1}, C_2 = 4.49 \times 10^{-2},$ and $C_3 = 1.56 \times 10^{-2}$



orientation (Figs. 2 and 8, S2–S4; Table 2). The stress and strain rate data (Fig. 7b), combined with the results of previous studies, indicate that deformation occurred by grain boundary diffusion creep (cf., $n \sim 1$, where $\dot{\epsilon} \propto \sigma^n$). When the sample deforms by this type of creep, the generation of defects that produce cores of nucleation for the transformation would be limited, which means we cannot see the effects of deformation on the transformation.

The prior grain sizes of PEn are different for the deformed and reference samples (Fig. 8a; Table 1), presumably due to the effect of the forsterite grain distribution, which can pin the grain boundary of enstatite. The grain sizes of forsterite and enstatite, and the forsterite fraction are consistent with the Zener relationship ($\frac{d_{\text{PEn}}}{d_{\text{Fo}}} = \frac{z}{f_{\text{Fo}}^{0.5}}$, where z is the Zener constant) with or without deformation (Fig. S6).

Ohi et al. (2022) reported that shear stress during sample preparation for XRD analysis affects the phase transition from PEn to CEn. They demonstrated that PEn powders pulverized with an agate mortar for 15 min were transformed to CEn. The fraction of CEn increased with

increasing pulverization. Ohi et al. (2022) also suggested that the transformations could have occurred during sample preparation (cutting and polishing) at room PT . Therefore, all the polished sections in this study were prepared one day prior to SEM and EBSD analyses, as explained in the section on methods, so that the effects of sample preparation on the phase transformation were uniform across all samples. These observations, combined with our experimental results, indicate that deformation by diffusion creep does not affect the phase transformation directly, whereas brittle deformation does.

Transformation twins

The EBSD map that shows the phase transformation involved the formation of twins (Fig. 3, S3). The misorientation axes and angles of neighboring CEn grains are characteristic of twins with a [100] or [001] rotation axis and a rotation angle of 180° (Fig. 4). The crystal structures of PEn and CEn (Fig. 9a) show that their b and c parameters are

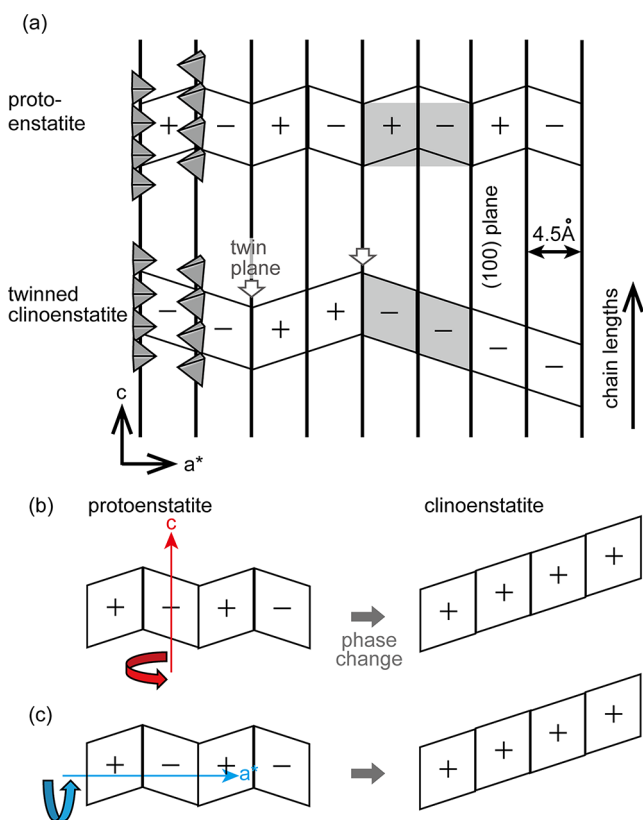


Fig. 9 (a) Crystal structures of protoenstatite and twinned clinoenstatite. Gray tetrahedra on the left side indicate the SiO₄ tetrahedra that form the chain structure of enstatite. White open arrows indicate the twin plane of clinoenstatite. Gray highlighted areas indicate the unit cell of the mineral. The image is modified from Buseck et al. (1980) and Putnis (1992). The possible mechanisms of transformation from PEn to CEn are shown in (b-c). The image is from Smyth (1974). (b) Rotation angle of $\approx 180^\circ$ around the [001] axis. (c) Rotation angle of $\approx 180^\circ$ around the [100] axis. There are two possible positions corresponding to the relative displacements of adjacent chains along their length, labeled + and -

similar, whereas a lattice parameter changes according to the arrangement of the chains (Buseck et al. 1980; Lee and Heuer 1987; Boysen et al. 1991; Putnis 1992). This implies that a possible transformation mechanism from PEn to CEn would be a rotation angle of 180° around the [100] or [001] axis (Fig. 9b-c). The SEM images and EBSD maps (Figs. 1, 3, S3) show polysynthetic twins in the CEn grains. The relationships between the fraction of protoenstatite and grain size (Fig. 8b), according to the theoretical model represented by Eq. (1), demonstrate that the phase transformation from PEn to CEn occurs from the lattice defects of volume nucleation. This assumption is consistent with the transformation mechanism proposed above (Fig. 9b-c). Similar transformation twins in CEn have also been observed in natural rocks such as boninite and meteorites (e.g., Smyth 1974; Shiraki et al. 1980).

Exploding samples due to the volume change of phase transformation

The samples sintered at 1360°C for > 1 h exploded after a period of time and became powders (Fig. S1; Supplementary material video 1) due to the volume change induced by the back-transformation of PEn. During the phase transformation from PEn to CEn, the volume changes by -5 to -6.1 vol% (Lee and Heuer 1987). The grain boundaries around enstatite grains with twins had cracks (Fig. 2). The XRD analyses (Fig. 6) show that the exploded samples have peaks of CEn and forsterite but an absence of PEn peaks. In contrast, the sample that did not explode (sintering time 1 h; sample 60S1) did not show any CEn peaks. These features are consistent with the assumption that the samples exploded as a result of the volume change during phase transformation. In a previous study using Raman microspectroscopy and a single crystal of PEn, Reynard et al. (2008) demonstrated that cracks formed due to the strain of the phase transformation. A similar type of exploding due to a martensitic phase transformation has also been reported in ceramic crystal aggregates (Gu et al. 2021).

The relationship between sintering time and grain size (Table 1) is consistent with the results of grain growth experiments undertaken by Tasaka and Hiraga (2013), who reported that static grain growth occurs via Ostwald ripening in experiments at 1260 – 1360°C with enstatite crystal aggregates, using the same sample preparation procedures and similar types of experimental setting as in the present study. Since the grain growth rate is a function of temperature, the samples sintered at a higher temperature (1360°C) have larger grain sizes than those sintered at a lower temperature (1345°C). Therefore, the samples sintered at 1360°C for > 1 h with a larger grain size were those that exploded due to the volume change induced by the back-transformation of PEn. The probability of transformation of PEn increases with increasing grain size (Sect. 4.1.).

Geological and mineralogical applications

As stated in the introduction, PEn is an unquenchable phase that transforms to twinned CEn in natural rocks (boninite and meteorites). Therefore, the typical occurrence of CEn and PEn in lower crustal and mantle rocks remain unclear. The stability field of PEn is within the range of $P < 1$ GPa and $T = 985$ – 1557°C , which corresponds to the PT conditions of young oceanic lithosphere.

PEn is the stable form of enstatite at high temperatures, but samples recovered from the experiments contain CEn due to the back-transformation of PEn (Lee and Heuer 1987; Reynard et al. 2008). Therefore, in previous studies, protoenstatite was synthesized by doping small amounts

of impurities using a flux method (Ozima 1982; Ohi et al. 2022). A similar technique, using a small amount of dopant to stabilize a high-temperature phase to prevent a martensitic transformation, has also been used in ceramic crystal aggregates (e.g., stabilized zirconia) (e.g., Matsui et al. 2023). In contrast, the enstatite used in the present study was highly pure with a trace element content of < 10 ppm (Koizumi et al. 2010), and the samples with a sintering time of 1 h (samples 45S1 and 60S1) had a mineral fraction of $f_{PEn} = 99\%$ (Fig. 8b). In addition, the samples were synthesized from nano-powder. These features indicate that the smaller grain size would be highly effective in preventing the back-transformation of enstatite.

The grain size distributions determined using SEM + EDS and EBSD (Fig. 5c, S5c) show that the average enstatite grain size becomes smaller after transformation, as clearly seen in the samples with sintering times of 10 and 50 h and the reference samples (samples 45S10, 45S50, 45S10D1r, 45S10D2r), even if the mechanism can be characterized as a second-order transformation. As the grain size decreases, the rheological properties change with ongoing deformation by grain size sensitive creep. The results of previous high-pressure experiments and numerical modeling studies have also led to suggestions that the strain-weakening process due to grain size reduction associated with transformation would occur in the Earth's interior (e.g., Solomatov and Reese 2008; Mohiuddin et al. 2020; Ohuchi et al. 2022).

Conclusions

We conducted grain growth and deformation experiments on enstatite aggregates to understand the microstructural developments during the phase transformation from protoenstatite to clinoenstatite. Based on our microstructural analyses, we conclude the following.

1. The grain growth experiments indicate that grain size influences the phase transition. The fraction of transformed clinoenstatite increases with increasing grain size, since the number of defects within a grain available to act as nucleation sites for the transformation changes with grain size, which is consistent with a previously proposed nucleation model for phase transformations. The samples sintered at 1360 °C for > 1 h exploded due to the volume change of the phase transformation. A possible mechanism for the transformation from protoenstatite to clinoenstatite is the formation of transformation twins that are defined by a rotation angle of 180° around the [100] or [001] axis. Grain sizes become smaller during the phase transformation, even
2. The deformation experiments indicated that deformation by diffusion creep does not affect the phase transition. We were not able to detect microstructural differences between deformed and reference samples in terms of grain size, grain shape, phase distribution, or crystallographic orientation. Combined with previous studies, deformation by diffusion creep does not affect the phase transformation directly, whereas brittle deformation does.

Supplementary Information The online version contains supplementary material available at <https://doi.org/10.1007/s00269-024-01294-5>.

Acknowledgements We thank S. Ohi for technical assistance during the enstatite analyses and for stimulating discussions. We thank T. Hiraga, S. Koizumi, T. Kawamoto, and M. Morishige for stimulating discussions. The nano-powder was supplied by T. Hiraga through a cooperative research program of the Earthquake Research Institute, University of Tokyo. The manuscript was improved by insightful comments from S. Demouchy, two anonymous reviewers, and the editor L. Dobrzhinetskaya. This research was supported by JSPS KAKENHI Grant JP22K18731 and ERI JURP Grant 2024-G-01 from the Earthquake Research Institute of the University of Tokyo. We acknowledge the support of research facilities provided by Shizuoka Instrumental Analysis Center, Shizuoka University.

Author contributions Miki Tasaka and Maya Iwago helped conceive and design this study. Material preparation and grain growth experiments were performed by Maya Iwago. The deformation experiments, data collection, and data analyses were performed by Maya Iwago and Miki Tasaka. The first draft of the manuscript was written by Miki Tasaka. All the authors commented extensively on the final version of the manuscript.

Data availability No datasets were generated or analysed during the current study.

Declarations

Competing interests The authors declare no competing interests.

References

- Boysen H, Frey F, Schrader H, Eckold G (1991) On the Proto- to Ortho-/Crino enstatite transformation: single crystal X-ray and inelastic neutron investigation. *Phys Chem Minerals* 17:629–635
- Buseck PR, Nord GL, Veblen DR (1980) Subsolidus phenomena in pyroxene, reviews in mineralogy 7 pyroxene. *Mineralogical Soc Am* 128–143
- Bystricky M, Lawlis J, Mackwell S, Heidelbach F, Raterron P (2024) High-temperature deformation of enstatite – olivine aggregates. *J Geophys Res Solid Earth* 129 e2023JB027699
- Chen IW, Chiao YH, Tsuzaki K (1985) Statistics of martensitic nucleation. *Acta Metall* 33 10:1847–1859
- Gu H, Rohmer J, Jetter J, Lotny A, Kienle L, Quandt E, James RD (2021) Exploding and weeping ceramics. *Nature* 599:416–420

- Hiraga T, Tachibana C, Ohashi N, and Sano S (2010a) Grain growth systematics for forsterite ± enstatite aggregates: Effect of lithology on grain size in the upper mantle. *Earth Planet Sci Lett* 291:10–20
- Hiraga T, Moyazaki T, Tasaka M, Yoshida H (2010b) Mantle superplasticity and its self-made demise. *Nature* 468:1091–1094
- Jones SA, Burlitch JM, Duchamp JC, Duncan TM (1999) Sol-gel synthesis of protoenstatite and a study of the factors that affect crystallization. *J Sol-Gel Sci Technol*, 201–209
- Kanzaki M, Xue X (2017) Protoenstatite in MgSiO₃ samples prepared by conventional solid state reaction. *J Mat Phy* 112:359–364
- Karato S (2008) Deformation of earth materials: an introduction to the rheology of solid earth. Cambridge University Press, pp 271–287
- Koizumi S, Hiraga T, Tachibana C, Tasaka M, Miyazaki T, Kobayashi T, Takamasa A, Ohashi N, Sano S (2010) Synthesis of highly dense and fine-grained aggregates of mantle composites by vacuum sintering of nano-size mineral powders. *Phys Chem Minerals* 37(8):505–518
- Lee WE, Heuer AH (1987) On the polymorphic of Earth. *J Am Ceram Soc* 70(5):349–360
- Matsui K, Hosoi K, Feng B, Yoshida H, Ikuhara Y (2023) Ultrahigh toughness zirconia ceramics. *PNAS* 120(27):e2304498120. <https://doi.org/10.1073/pnas.2304498120>
- Mohiuddin A, Karato S, Girard J (2020) Slab weakening during the olivine to ringwoodite transition in the mantle. *Nat Geo*. <https://doi.org/10.1038/s41561-019-0523-3>
- Ohi S, Miyake A (2016) Phase transitions between high- and low-temperature orthopyroxene in the Mg₂Si₂O₆ – Fe₂Si₂O₆ system. *Am Min* 101:1414–1422
- Ohi S, Miyake A, Yashima M (2010) Stability field of the high-temperature orthorhombic phase in the enstatite-diopside system. *Am Min* 95:1267–1275
- Ohi S, Osako T, Miyake A (2022) Effects of grain size, cooling rate, and sample preparation on the phase transition from protoenstatite to clinoenstatite. *Can Mineral* 60:1–12
- Ohuchi T, Higo Y, Tange Y, Sakai T, Matsuda K, Irifune T (2022) In situ X-ray and acoustic observation of deep seismic faulting upon phase transitions in olivine. *Nat Communication*. <https://doi.org/10.1038/s41467-022-32923-8>
- Ozima M (1982) Growth of orthoenstatite crystals by the flux method. *J Japanese Association Mineralogists Petrologists Economic Geol Special Paper* 3:97–103 (in Japanese)
- Presnall D (1995) *Mineral Physics & Crystallography: A Handbook of Physical Constants*, edited by T. Ahrens, AGU, p.248
- Putnis A (1992) *Introduction to mineral sciences*. Camb Univ Press 141–184
- Reynard B, Bass JD, Jackson JM (2008) Rapid identification of state-enstatite polymorphs at various temperature. *J Eur Ceram Soc* 28:2459–2462
- Shiraki K, Kuroda N, Urano H, Maruyama S (1980) Clinoenstatite in boninites from Bonin island, Japan. *Nature* 285:31–32
- Smyth JR (1974) Experimental study on the polymorphism of enstatite. *Am Min* 59:345–352
- Solomatov VS, Reese CC (2008) Grain size variation in the Earth's mantle and the evolution of primordial chemical heterogeneities. *J Geophys Res Solid Earth* 113:B07408
- Tasaka M, Hiraga T (2013) Influence of mineral fraction on the rheological properties of forsterite + enstatite during grain-size-sensitive creep: 1. Grain size and grain growth laws. *J Geophys Res Solid Earth* 118:3970–3990
- Tasaka M, Hiraga T, Zimmerman ME (2013) Influence of mineral fraction on the rheological properties of forsterite + enstatite during grain-size-sensitive creep: 2. Deformation experiments. *J Geophys Res Solid Earth* 118:3991–4012
- Tasaka M, Maeda K, Nambu K, Motomura H, Yoshida H (2023) Sintering and deformation properties of forsterite + diopside aggregates in an electrical field. *Phys Earth Planet Inter* 341:107051

Publisher's Note Springer Nature remains neutral with regard to jurisdictional claims in published maps and institutional affiliations.

Springer Nature or its licensor (e.g. a society or other partner) holds exclusive rights to this article under a publishing agreement with the author(s) or other rightsholder(s); author self-archiving of the accepted manuscript version of this article is solely governed by the terms of such publishing agreement and applicable law.